Electronic Supplementary Material (ESI) for Journal of Materials Chemistry A.

Supporting Information

Boosting Electrochemical Water Splitting via Ternary NiMoCo Hybrid Nanowire Arrays

Kailong Hu,[a] Mingxing Wu,[a] Satoshi Hinokuma,[b, c, d] Tatsuhiko Ohto,[e, *] Mitsuru Wakisaka,[d, f] Jun-ichi Fujita,[a] and Yoshikazu Ito[a, d, *]

[a] Institute of Applied Physics, Graduate School of Pure and Applied Sciences, University of Tsukuba, 1-1-1 Tennodai, Tsukuba 305-8571, Japan

[b] Department of Applied Chemistry and Biochemistry, Graduate School of Science and Technology, Kumamoto University, 2-39-1 Kurokami, Kumamoto 860-8555, Japan

[c] International Research Organization for Advanced Science and Technology, 2-39-1 Kurokami, Kumamoto 860-8555, Japan

[d] PRESTO, Japan Science and Technology Agency, Saitama 332-0012, Japan

[e] Graduate School of Engineering Science, Osaka University, 1-3 Machikaneyama, Toyonaka 560-8531, Japan

[f] Graduate School of Engineering, Toyama Prefectural University, 5180 Kurokawa, Imizu, Toyama 939-0398, Japan

Corresponding Author

*E-mail: ito.yoshikazu.ga@u.tsukuba.ac.jp; ohto@molectronics.jp

Experimental methods

Preparation of $NiMoO_4$ nanofibers coated on Ni foam

As-received Ni foam (1.0 cm^2) was similarly treated as mentioned above. After that, the treated Ni foams were put into a 50 ml Teflon coated stainless autoclave with 1.5 mmol $NiCl_2 \cdot 6H_2O$ (98% purity, Wako), 1.5 mmol $Na_2MoO_4 \cdot 2H_2O$ (99% purity, Wako), and 30 mL ultrapure water. The hydrothermal procedure was performed at 150 °C for 6 hours. The obtained $NiMoO_4$ coated Ni foams were washed by ultrapure water several times to remove impurities. The loading amount of $NiMoO_4$ on a 1.0 cm^2 Ni foam after drying was 2.8±0.3 mg.

Calculation of turnover frequency (TOF)

The TOF values were calculated by CV tests with a sweep rate of 50 mV s^{-1} at potentials ranging from −200 to +600 mV (vs. RHE) for HER and +800 to +1600 mV (vs. RHE) for OER in 1.0 M KOH electrolyte.[1] Assuming a one electron process,[2] the integrated charge (Q) obtained for the entire potential region should be divided by two, and the Faraday constant F (96485 C mol^{-1}). Thus, the active sites for samples were calculated as following,[3]

$$\mathrm{n} = \frac{Q}{2\mathrm{F}}$$

The TOF value (s^{-1}) can be estimated via the equation below,

$$\mathrm{TOF} = \frac{I}{2 \text{ or } 4\mathrm{F}n}$$

where I and n are the current (A) at an electrode potential and the number of active sites (mol). The number of 2 or 4 represents two or four electrons transfer to obtain one H_2 or O_2 molecule, respectively.

Faradaic efficiency

H_2 and O_2 gases generated on the cathode and anode were separately collected, and the volumes were compared with the theoretical values. The theoretical yields of H_2 and O_2 were simply calculated using the equation as following,[2, 4]

$$V_{\mathrm{H2}}\ (\mathrm{mL}) = Q\ (\mathrm{C}) \times 22.4\ (\mathrm{L\ mol^{-1}}) \times 1000 / 2 \times \mathrm{F}\ (\mathrm{C\ mol^{-1}})$$

$$V_{\mathrm{O2}}\ (\mathrm{mL}) = Q\ (\mathrm{C}) \times 22.4\ (\mathrm{L\ mol^{-1}}) \times 1000 / 4 \times \mathrm{F}\ (\mathrm{C\ mol^{-1}})$$

The Faradaic efficiency was estimated by comparing the amount of experimentally quantified volume of H_2 and O_2 gas with theoretically calculated gas volume.

Inductively coupled plasma measurements for leaching test

One piece of 1.0×1.0 cm^2 CC@NiMoCo sample was dissolved in 1.0 M HNO_3 solution. The carbon cloth was chosen as the substrate to avoid inaccuracy of Ni atomic concentration, because HNO_3 solution may dissolve additional Ni from Ni foam. This solution was analyzed by inductivity coupled plasma optical emission spectrometer (ICP−OES, ICPS−8100, Shimazu) to determine the weight ratio of Ni, Mo, and Co in a piece of 1.0×1.0 cm^2 sample, respectively. Then, two pieces of 1.0×1.0 cm^2 NF@NiMoCo samples were set as cathode and anode, and the electrolyte was collected periodically for leaching check during long-term stability test. The leaching ratio of Ni was calculated using the equation as below,

$$\text{Leaching rate (\%)} = \frac{\text{Ni concentration in solution (mg/L)} \times \text{solution volume (L)}}{\text{Ni amount in NF@NiMoCo sample (mg)}} \times 100\%$$

The calculation method of Mo and Co was similarly performed.

Computational protocols

(1) Density functional theory set up and surface preparations

The first-principles calculations were performed with the VASP code.[5] We used the projected augmented wave (PAW) method.[6] For the exchange and core-functional, we used Perdew-Burke-Ernzerhof (PBE) functional.[7] The plane wave energy cutoff was set to 400 Ry. The dispersion correction was included via the Grimme's D3 (BJ) method.[8, 9]

We investigated a NiMo surface and two $NiMo_2Co$ surfaces to determine their catalytically active sites. As previous,[10] we assumed that the NiMo system forms δ-phase NiMo: $Ni_{24}(Ni_4Mo_{16})Mo_{12}$,[11, 12] and its (100) face forms the surface of the NiMo system. The lattice constant of the NiMo(100) surface is 8.852 Å × 9.108 Å.[11, 12]

Since the precise structure of $NiMo_2Co$ (JCPDS 00-009-0298) is not obtained, we constructed the bulk structure based on the modifications of Mo_6Co_7,[13] which has same symmetry (R-3m(166)) with $NiMo_2Co$. We replaced three Co atoms with Ni and deleted one Co atom from the unit cell. Then, we have tried several patterns for the replacement and adopted the most stable structure as a $NiMo_2Co$ (the CIF file is given). Figure S29, S30 and Table S5 show the comparison of XRD and EXAFS results with experimental $NiMo_2Co$ (JCPDS 00-009-0298) and the modified $NiMo_2Co$ structures. The most featured peaks such as (027) and (116) are well captured. Because the original (027) and (116) surfaces are very large, we picked the smaller cells as shown in Figure S20 and S21 and named them as (027)' and (116)', where the lattice constants of the surface unit cells are 9.49 Å × 19.85 Å and 13.70 Å × 9.89 Å, respectively. The vacuum layer of about 20 Å was inserted to avoid the interaction between the mirror cells.

(2) Evaluation of energy diagrams

The hydrogen adsorption energy (ΔE_{H*}) was calculated as:

$$\Delta E_{\mathrm{H}*} = \frac{1}{n}(E_{\mathrm{tot}} - E_{\mathrm{sub}}) - \frac{1}{2}E_{\mathrm{H}_2} \qquad (1)$$

where E_{tot} is the total energy of the substrate with *n* hydrogen atoms adsorbed on the surface, E_{sub} is the total energy of the substrate, and E_{H_2} is the energy of a hydrogen molecule in the gas phase (about −6.7eV was employed in this work). The Gibbs free energy for the hydrogen absorption was corrected as:

$$\Delta G_{\mathrm{H}} = \Delta E_{\mathrm{H}*} + \Delta E_{\mathrm{ZPE}} - T\Delta S_{\mathrm{H}}, \qquad (2)$$

where ΔE_{ZPE} is the difference in zero-point energy between the adsorbed hydrogen and hydrogen in the gas phase and ΔS_{H} is the entropy difference between the adsorbed state and the gas phase. As the contribution from the vibrational entropy of H* in the adsorbed state is negligibly small, the entropy of hydrogen adsorption is $\Delta S_{\mathrm{H}*} \approx -\frac{1}{2}S_{\mathrm{H}_2}$, where S_{H_2} is the entropy of H_2 in the gas phase. Then the Gibbs free energy with the overall corrections can be calculated as $\Delta G_{\mathrm{H}*} = \Delta E_{\mathrm{H}*} + 0.24$ eV.

For the oxygen evolution reaction, we considered the four elementary steps:[14, 15]

$$\mathrm{H_2O_{(l)}} + * \rightarrow \mathrm{OH}* + \mathrm{H}^+/e^- \qquad (3)$$

$$\mathrm{OH}* \rightarrow \mathrm{O}* + \mathrm{H}^+/e^- \qquad (4)$$

$$\mathrm{O}* + \mathrm{H_2O_{(l)}} \rightarrow \mathrm{OOH}* + \mathrm{H}^+/e^- \qquad (5)$$

$$\mathrm{OOH}* \rightarrow \mathrm{O_2(g)} + * + \mathrm{H}^+/e^- \qquad (6)$$

where * represents a surface site and OH*, O*, and OOH* are intermediates adsorbed on an active site on the catalyst surface. The free energy of each intermediate is calculated at 0 V vs standard hydrogen electrode by referencing liquid water and hydrogen gas at standard conditions:

$$\Delta G_{\mathrm{OH*}} = E_{\mathrm{OH*}}^{\mathrm{DFT}} - E_{*}^{\mathrm{DFT}} - E_{\mathrm{H_2O}}^{\mathrm{DFT}} + \frac{1}{2}E_{\mathrm{H_2}}^{\mathrm{DFT}} + \hat{G}_{\mathrm{OH}} \tag{7}$$

$$\Delta G_{\mathrm{O*}} = E_{\mathrm{O*}}^{\mathrm{DFT}} - E_{*}^{\mathrm{DFT}} - E_{\mathrm{H_2O}}^{\mathrm{DFT}} + E_{\mathrm{H_2}}^{\mathrm{DFT}} + \hat{G}_{\mathrm{O}} \tag{8}$$

$$\Delta G_{\mathrm{OOH*}} = E_{\mathrm{OOH*}}^{\mathrm{DFT}} - E_{*}^{\mathrm{DFT}} - 2E_{\mathrm{H_2O}}^{\mathrm{DFT}} + \frac{3}{2}E_{\mathrm{H_2}}^{\mathrm{DFT}} + \hat{G}_{\mathrm{OH}} \tag{9}$$

where E_{*}^{DFT}, $E_{\mathrm{OH*}}^{\mathrm{DFT}}$, $E_{\mathrm{O*}}^{\mathrm{DFT}}$, and $E_{\mathrm{OOH*}}^{\mathrm{DFT}}$ are the ground state energy of the surface and the surface with OH*, O*, and OOH* intermediates, respectively. $E_{\mathrm{H_2O}}^{\mathrm{DFT}}$ and $E_{\mathrm{H_2}}^{\mathrm{DFT}}$ are the energies of H_2O and H_2 molecules, respectively, in the gas phase. $\hat{G}$ includes contributions from vibration energy and entropy of the intermediate at 300 K. We employed typical values of 0.35 eV, 0.05 eV, and 0.40 eV for OH*, O*, and OOH*, respectively.[14, 15] The standard free energy change of each elementary step can be calculated:

$$\Delta G_1^{\mathrm{o}} = \Delta G_{\mathrm{OH*}} \tag{10}$$

$$\Delta G_2^{\mathrm{o}} = \Delta G_{\mathrm{O*}} - \Delta G_{\mathrm{OH*}} \tag{11}$$

$$\Delta G_3^{\mathrm{o}} = \Delta G_{\mathrm{OOH*}} - \Delta G_{\mathrm{O*}} \tag{12}$$

$$\Delta G_4^{\mathrm{o}} = \Delta G_{\mathrm{O_2(g)}}^{\mathrm{o}} - \Delta G_{\mathrm{OOH*}} \tag{13}$$

$$\Delta G_{\mathrm{O_2(g)}}^{\mathrm{o}} = 4.92\ \mathrm{eV} \tag{14}$$

(3) Adsorption configurations of intermediates

The $\Delta G_{\mathrm{OOH*}}$ was large for all the surfaces studied in this DFT work so that the reaction process of (5) was not proceeded and the OOH* is easily decomposed into O and OH species, remaining on the surfaces. Therefore, we repeatedly adsorbed OOH* and performed the oxidation of the surface with the remained O* and OH* spices until it kept the molecular form after the optimization. Then we replaced OOH* with O* or OH* to estimate the adsorption free energies. The optimized adsorption structures were employed for calculating each energy diagrams (Figure 4, Table 1 and S3) and molecular adsorption model as illustrated in Figures S24-S26.

Supporting discussions

(1) Co atomic concentration dependence of HER/OER performances.

The morphologies of the NiMoCo alloy samples with various Co atomic concentrations were observed by SEM (Figure S7). The Co atomic concentration give significant influences on the morphology. With the increasing of Co atomic concentration, the sample morphology transformed from a flower-like nanowire array (Figure S7e) to nanosheet arrays with a sphere structure (Figure S7k). Each sample with different Co atomic concentrations were investigated by XPS measurements. The XPS results revealed that NiMoCo samples with different Co atomic concentrations (at.%), including 10.8 at.%, 19.3 at.%, 29.4 at.%, and 35.9 at.% on the surface (Figure S8a). Compared with Co-free NiMo alloy sample, the sample with 10.8 at.% and 19.3 at.% Co achieved superior HER activity, while the performance decreased with further increasing the Co atomic concentration (Figure S8b). Moreover, the NiMoCo alloy samples with Co atomic concentration ranging from 10.8 at.% to 35.9 at.% exhibited higher OER performances than that of Co-free NiMo alloy sample (Figure S8c). Thus, proper Co atomic concentration plays an important role in the enhancement of HER/OER performance. Both HER and OER experimental results indicate 19.3 at.% Co addition achieved the best HER/OER performance as summarized in Figure S8d.

(2) Leaching measurements of Ni, Mo and Co during overall water-splitting process

The leaching ratios of Ni, Mo, and Co during overall water-splitting test (70 hours) were measured to investigate the chemical stability of NF@NiMoCo. First, the total chemical composition of NiMoCo alloy was measured. Second, the leaching ratios of Ni, Mo, and Co elements during long-term overall water-splitting test were checked through measuring the element concentrations in the electrolyte. As indicated in Figure S17, the leaching ratio of Ni and Mo was approximately 2 wt.% and 18 wt.%, respectively, while the Co concentration (wt.%) in electrolyte was less than the detection limitation of 0.2 ppm. The metal leaching ratios after several hours became stable, and it is expected that the structures of electrode are preserved.

(3) HER and OER performances in 30 wt% KOH

Since 30 wt.% (7.64 M) KOH electrolyte is the widely used electrolyte in industrial alkaline electrolyzers, the HER/OER performances and electrochemical impedance spectroscopy (EIS) values of NF@NiMoCo sample were tested in 30 wt.% KOH electrolyte. Both HER and OER catalytic activities of NF@NiMoCo in 30 wt.% KOH electrolyte were superior to that in 1.0 M KOH electrolyte (Figures S18a and S18b). From the Nyquist plots in Figures S18c and S18d, the smaller solvent resistance (R_s) and charge transfer resistance (R_{ct}) values were achieved in 30 wt.% KOH electrolyte, which benefits the enhancement of the overall reaction kinetics of HER and OER processes as well as the energy efficiency. Moreover, the long-term water splitting test was performed using a couple of NF@NiMoCo electrodes in 30 wt.% KOH electrolyte in comparison with in 1.0 M KOH electrolyte (Figure S19a). The overall water splitting performance in 30 wt.% KOH electrolyte was higher than that in 1.0 M KOH electrolyte, while the chemical stability slightly decreased probably due to the more violent reaction procedures in 30 wt.% KOH electrolyte. The SEM images of NF@NiMoCo samples after the long-term water splitting test are showed in Figures S19b-e. The NiMoCo nanowire surface did not show large morphological changes on the HER process and show slight dissolution of the nanowires on the OER process in 30 wt.% KOH electrolyte in comparison to that in 1.0 M KOH electrolyte.

(4) Contribution of $NiMoO_4$ on HER/OER performance

Metal oxide catalysts are often employed for OER catalysts.[18] In the NF@NiMoCo sample, $NiMoO_4$ was detectedby the XRD measurement. Therefore, we investigated catalytic activity of $NiMoO_4$ to exclude its contributions toward HER/OER activity from the NF@NiMoCo sample. We synthesized only $NiMoO_4$ nanofibers on NF substrate (NF@$NiMoO_4$). The morphology and chemical composition of NF@$NiMoO_4$ were measured by SEM and XRD (Figures S23a and S23b). The SEM images showed that $NiMoO_4$ nanofibers were homogeneously coated on the surface of the NF substrate. The XRD peaks matched with the standard card of $NiMoO_4 \cdot xH_2O$ (JCPDS 00−013−0128). The HER and OER performances of NF@$NiMoO_4$ were investigated under similar experimental conditions for a fair comparision. The polarization curves (Figures S23c and S23d) showed that overpotentials of 191mV and 350mV (vs. RHE) were needed for the NF@$NiMoO_4$ sample to achieve HER/OER current density of 10 mA cm^{-2}, which is much larger than that of the NF@NiMoCo sample. This means that the outstanding HER/OER activity of NF@NiMoCo is mainly ascribed to NiMoCo alloy rather than $NiMoO_4$.

(5) Comparison of Ni foam substrate and carbon cloth substrate on HER/OER performances.

Generally, different substrates as catalyst supporters have different electrical conductivity and morphologies. These properties strongly affect HER/OER activity of catalysts coated on the substrate.[16, 17] In this study, we have investigated the substrate effects for the coated NiMoCo alloy catalysts to understand the differences of catalytic abilities between common substrates, i.e. Ni foam (NF, Celmet No. 8, Sumitomo Electric) and carbon cloth (CC, MOUBIC Inc.).

The characteristics and electrochemical performances of NiMoCo alloy coated on CC substrate (CC@NiMoCo) were shown in Figure S3b and S27. Noticeably, the CC@NiMoCo also have similar porous nanowires on the carbon cloth (Figure S27a and S27b). Thus, hierarchical architectures with primary porous structures provided by CC and secondary porous structures on the nanowires were confirmed. The crystal structures of CC@NiMoCo were indexed as $NiMo_2Co$ (116), $NiMo_2Co$ (027), NiMo (032), NiMo (231), and NiMo (041), which are identical with that of NF@NiMoCo (Figure S3). The CC@NiMoCo was tested by XPS measurements (Figure S28). The high resolution Ni 2p spectrum showed main peaks at 852.2 and 855.6 eV indexed as Ni^0 and Ni^{2+}. The Mo 3d spectrum deconvoluted into Mo^0 (227.4 and 230.6 eV), Mo^{4+} (228.7 and 231.8 eV), Mo^{5+} (230.3 and 233.4 eV), and Mo^{6+} (232.2 and 235.3 eV). The Co 2p spectrum could be assigned for Co^0 (777.7 and 792.6 eV) and Co^{2+} (780.4 and 796.6 eV). Therefore, the NiMoCo alloy samples coated on NF and CC are almost identical, and the only difference is the substrate.

The catalytic properties of NiMoCo catalysts on NF and CC were investigated under same lording amount of 3.0 mg per 1.0 cm^2 (3.0 mg/cm^2). The NF@NiMoCo sample exhibited better HER and OER performances than that of CC@NiMoCo (Figures S27c and S27d). The NF@NiMoCo sample achieved a HER/OER current density of 10 mA cm^{-2} at an overpotential of 23mV/277mV (vs. RHE), whereas the CC@NiMoCo sample needed 32mV/317mV (vs. RHE) to reach the same current density of 10 mA cm^{-2}. These differences were attributed to the faster electron transport ability of the NF substrate to NiMoCo catalysts coated on the surface.

Supporting figures

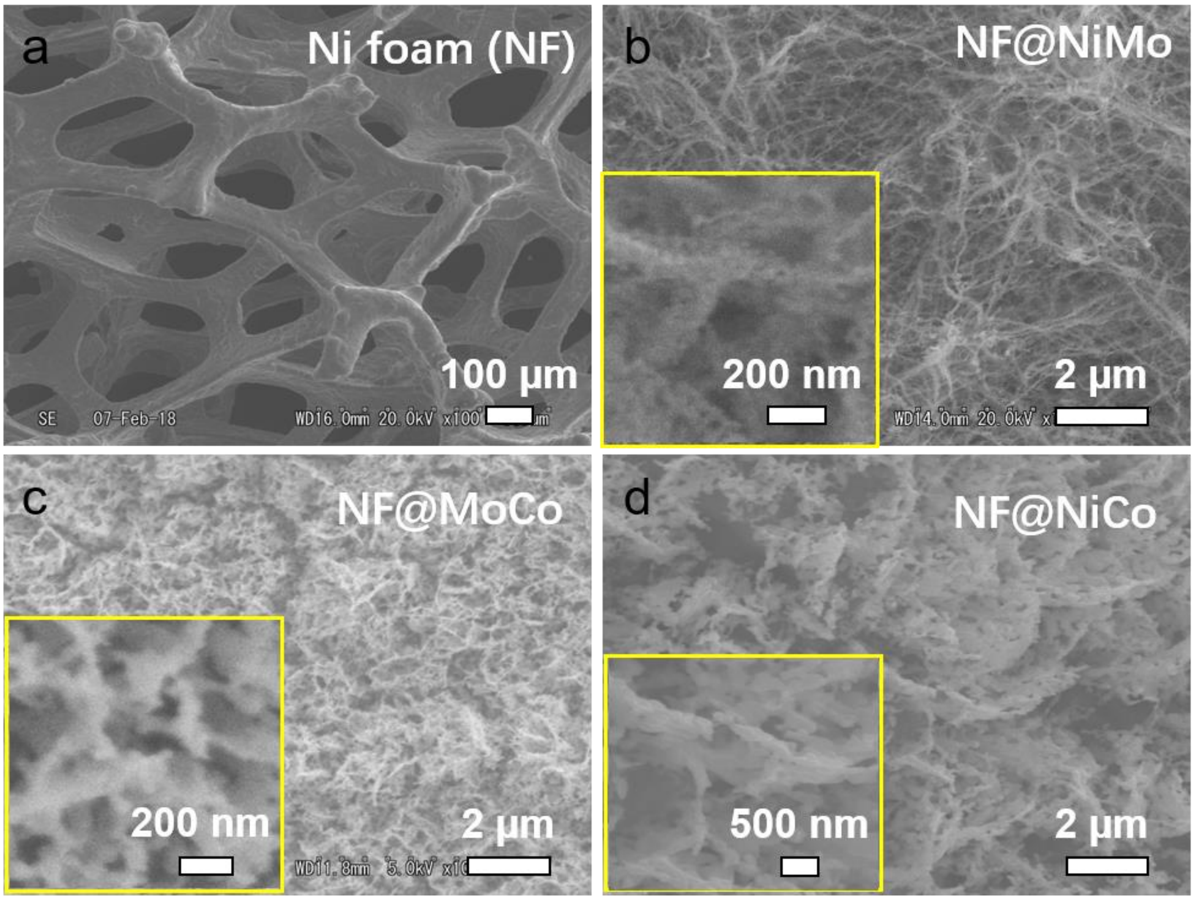

Figure S1. Surface morphologies of (a) Ni foam (as-received), (b) NF@NiMo, (c) NF@MoCo, and (d) NF@NiCo.

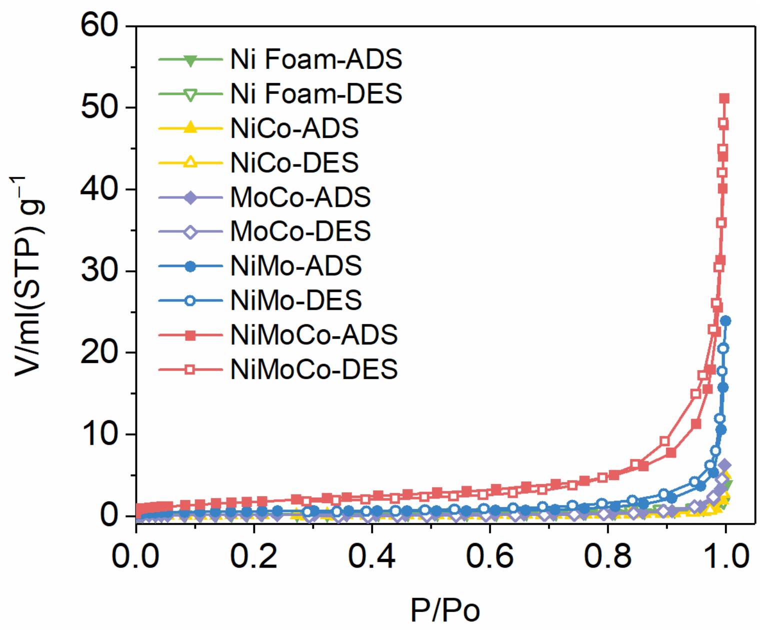

Figure S2. Nitrogen absorption and desorption measurements of as-synthesized electrocatalysts. The surface area was 6.48, 2.02, 0.45, 0.39, and 0.30 m^2 g^{-1} for NF@NiMoCo, NF@NiMo, NF@MoCo, NF@NiCo, and Ni foam (as-received), respectively.

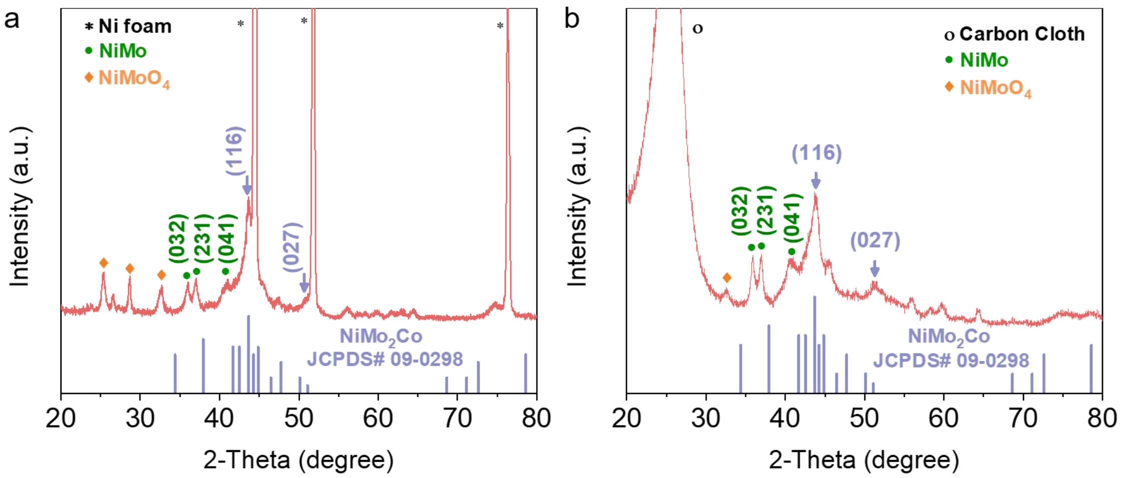

Figure S3. XRD patterns of (a) NF@NiMoCo and (b) CC@NiMoCo. The XRD pattern of CC@NiMoCo shows a clearer peak of $NiMo_2Co$ due to no intensity influence of Ni foam.

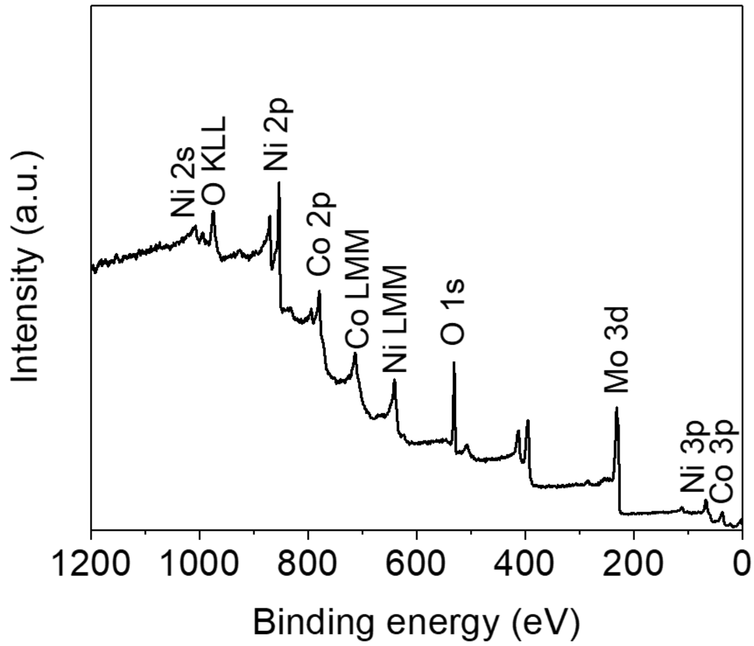

Figure S4. XPS spectrum of NF@NiMoCo.

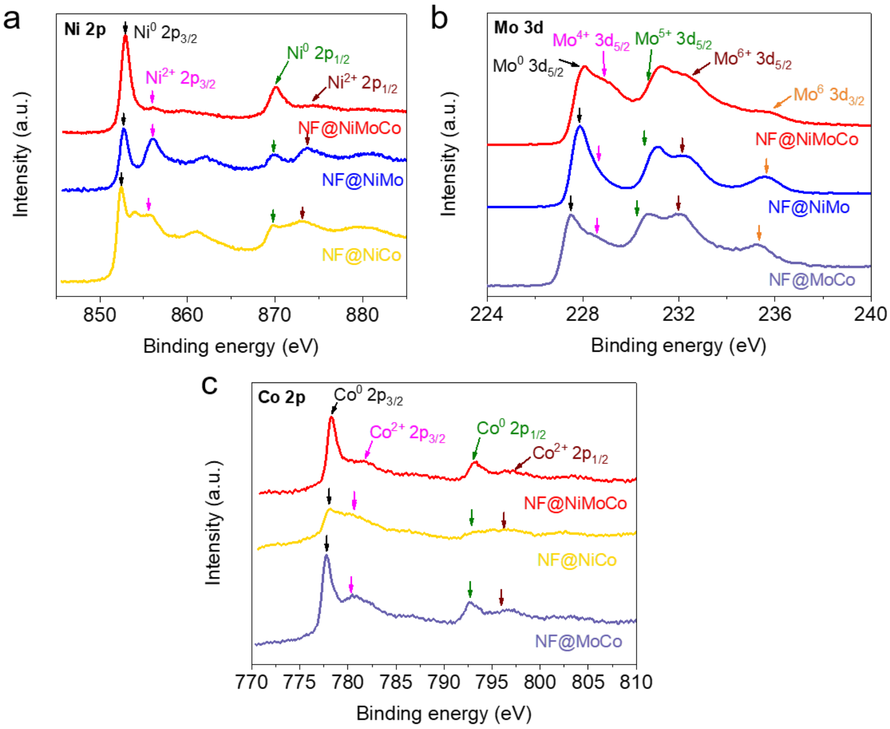

Figure S5. High-resolution (a) Ni 2p, (b) Mo 3d, and (c) Co 2p XPS spectra of NF@NiMo, NF@MoCo and NF@NiCo.

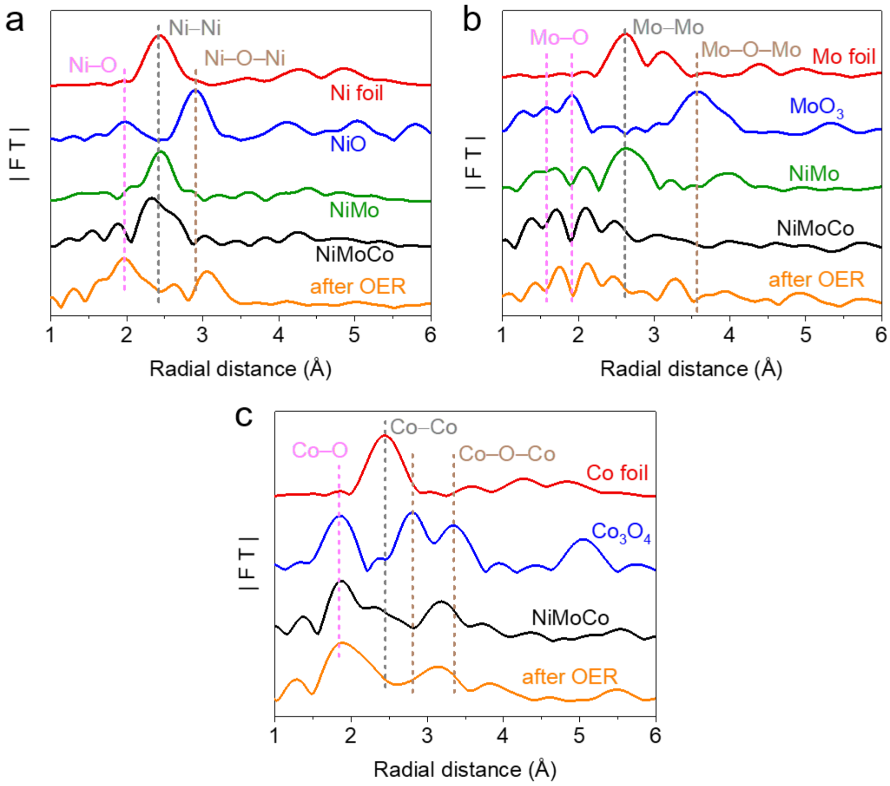

Figure S6. The Fourier transformed magnitudes of the EXAFS data for NiMo and NiMoCo nanowires coated on CC and NiMoCo sample after OER test. FT curves of (a) Ni K-edge, (b) Mo K-edge, and (c) Co K-edge EXAFS.

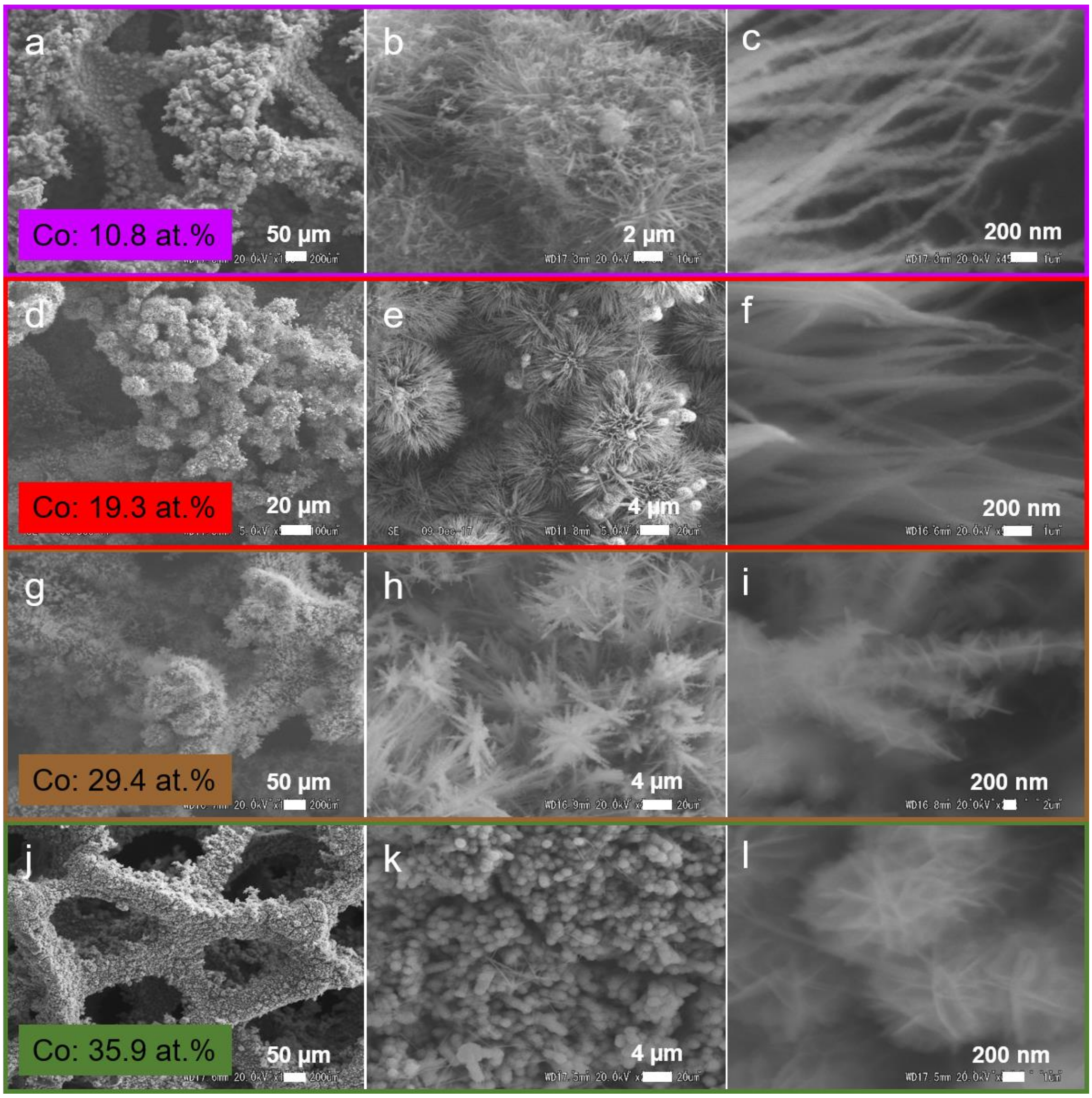

Figure S7. SEM images of NF@NiMoCo samples with various Co atomic concentrations. The Co atomic concentration on the sample surface was confirmed by XPS measurements.

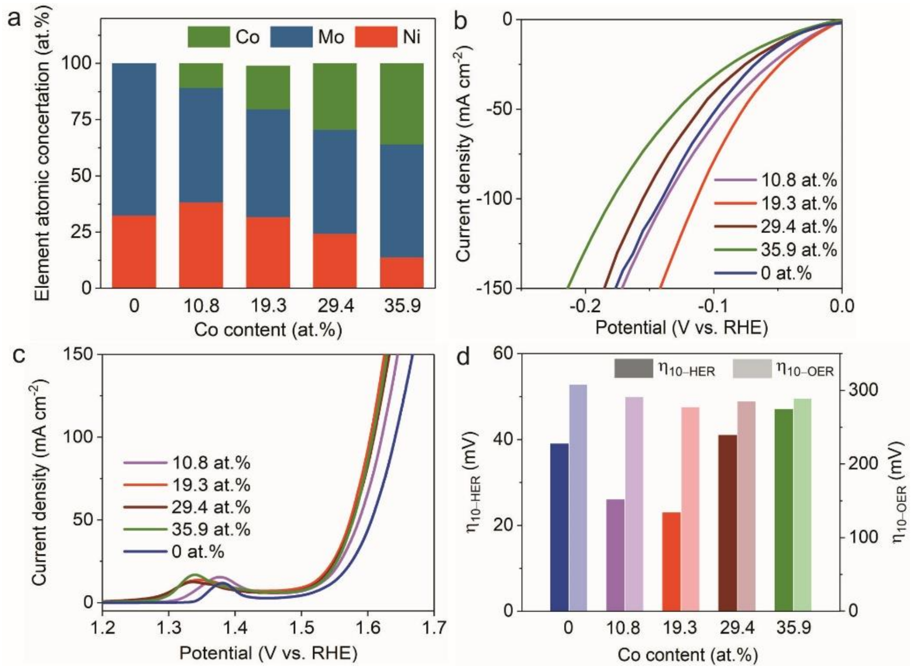

Figure S8. (a) The Ni, Mo and Co atomic concentrations of various samples coated on Ni foam. The "Co 0 at.%" represents the Co-free NF@NiMo sample. The number in the green column represents the Co concentration (at.%). (b) HER, (c) OER polarization curves and (d) summary of η_{10-HER} and η_{10-OER} values of samples with different Co atomic concentrations.

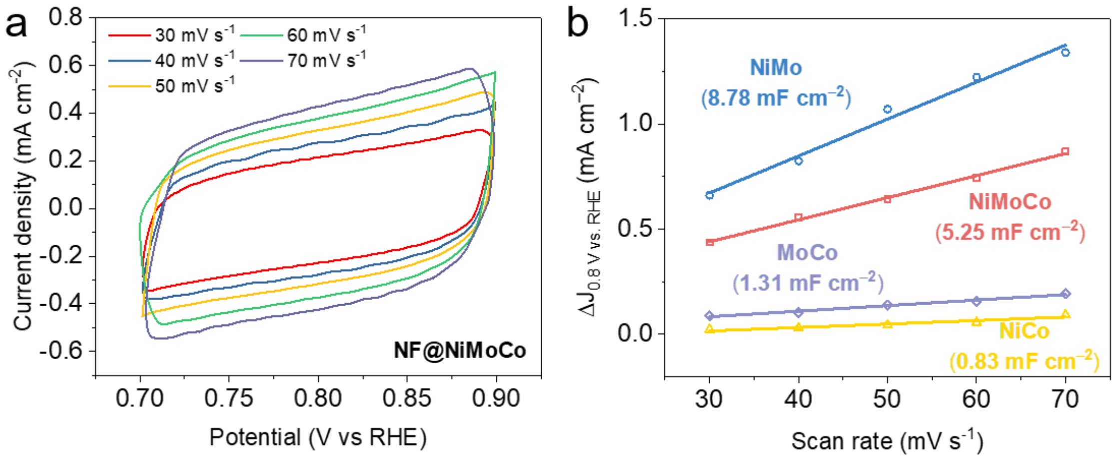

Figure S9. Typical cyclic voltammograms in the region of +700 to +900 mV (vs. RHE) with different sweep rates for (a) NF@NiMoCo. (b) Capacitive current density plotted against various sweep rates of NF@NiMoCo, NF@NiMo, NF@MoCo, and NF@NiCo.

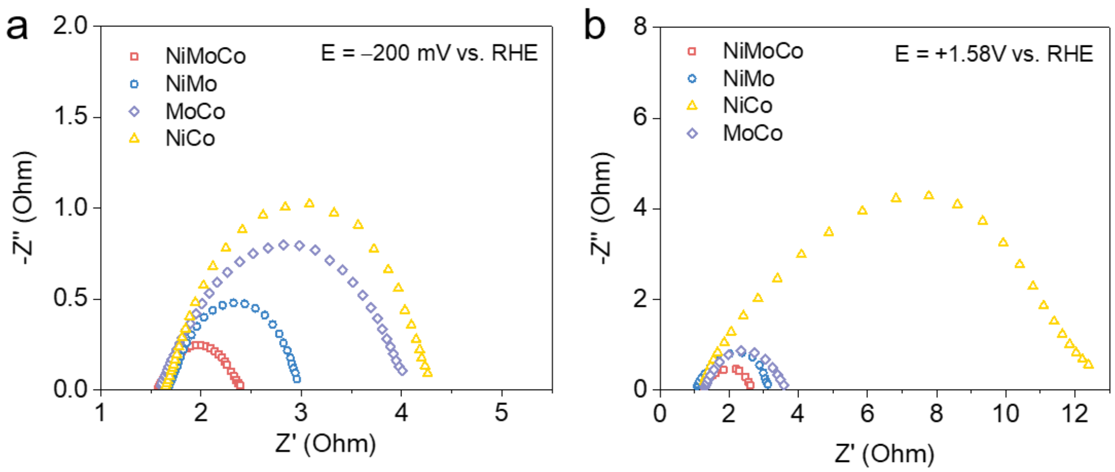

Figure S10. Nyquist plots of NF@NiMoCo, NF@NiMo, NF@MoCo, NF@NiCo at potential of (a) −200 mV vs. RHE and (b) +1.58 V vs. RHE.

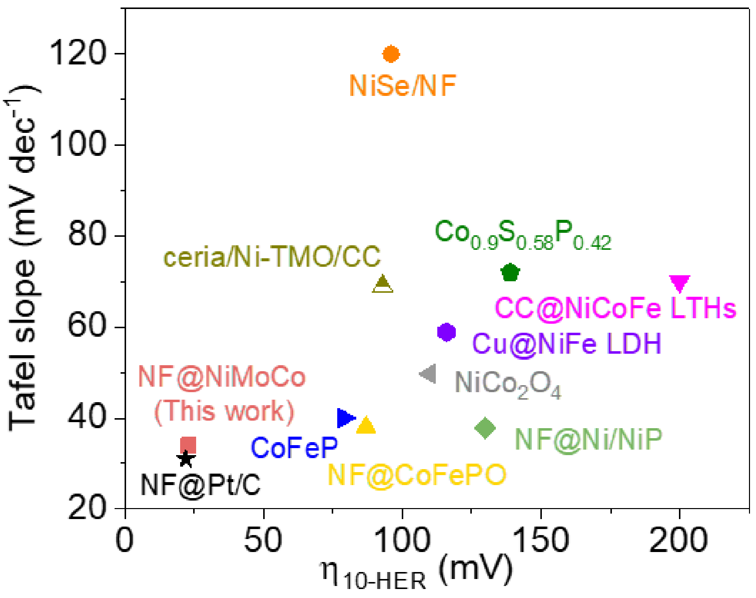

Figure S11. Comparison of $\eta_{10\text{−HER}}$ values and Tafel slopes with other recently reported water-splitting catalysts.[19, 20, 21-26]

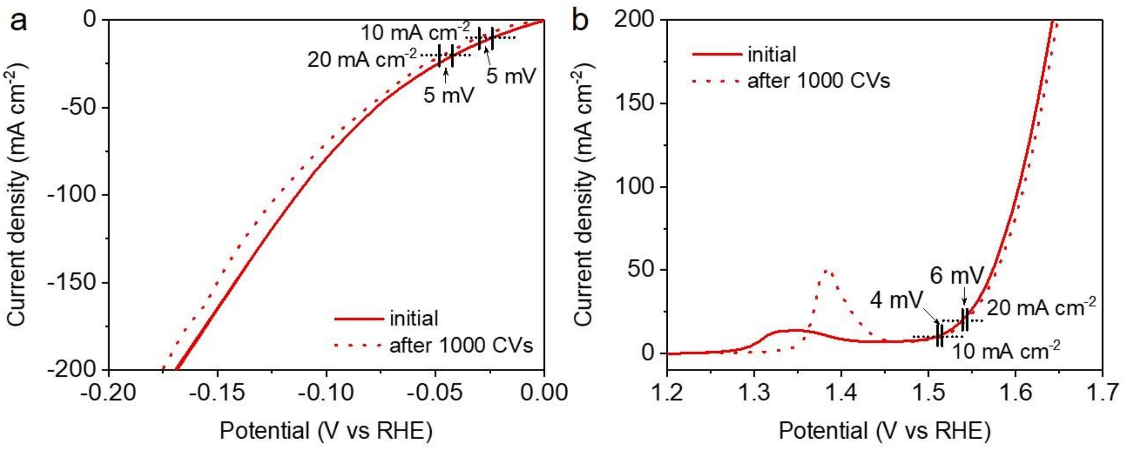

Figure S12. Polarization curves of NF@NiMoCo before and after 1000 CV cycles during (a) HER and (b) OER processes.

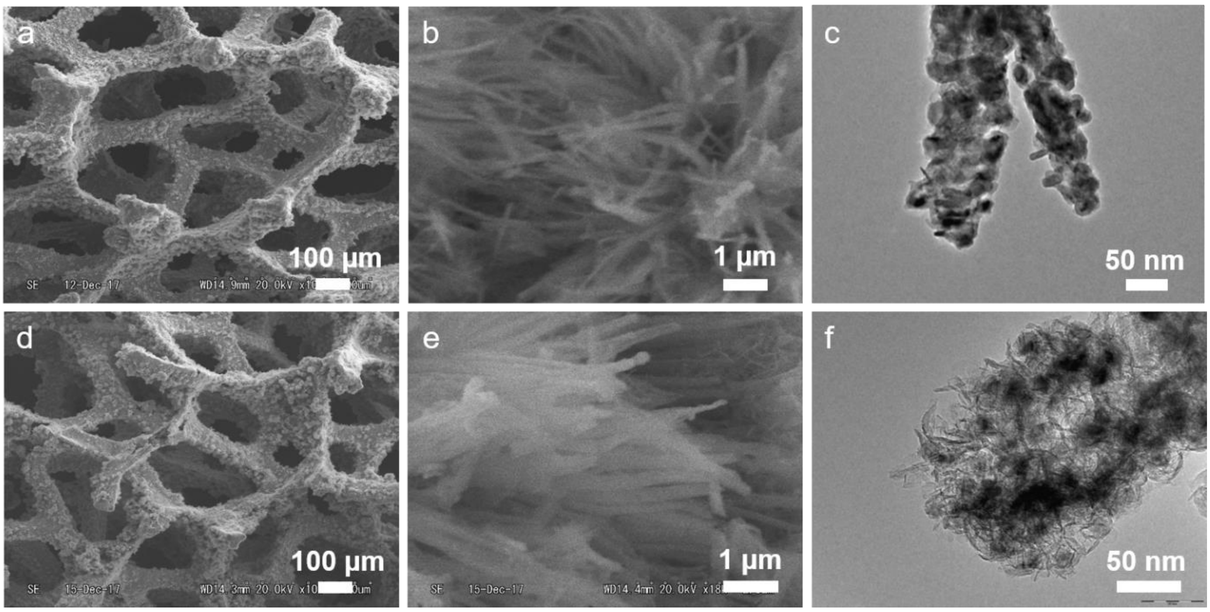

Figure S13. Morphology of NF@NiMoCo after one-day (a-c) HER and (d-f) OER durability (CA) test.

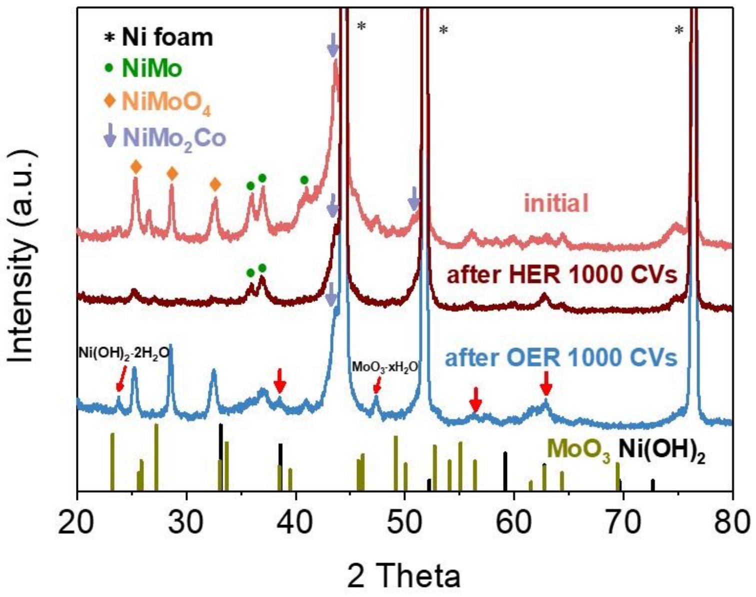

Figure S14. The XRD patterns of NF@NiMoCo after HER and OER stability tests. The XRD patterns demonstrated that the NF@NiMoCo sample after HER test retained most of metallic phases, such as NiMo and NiMo$_2$Co. The self-formation of nickel and molybdenum oxide/hydroxide species during OER procedure was further confirmed in XRD pattern of sample after OER test (marked by red arrows), which corresponds with XPS and XANES spectra (Figures S15 and S16).

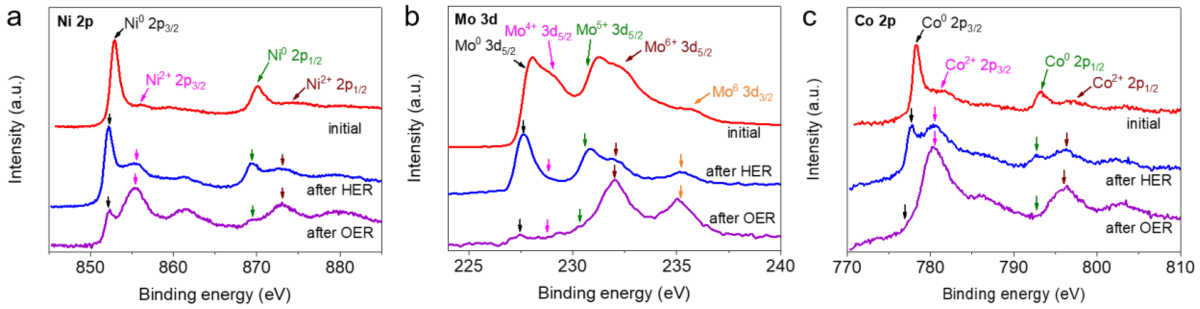

Figure S15. High-resolution (a) Ni 2p, (b) Mo 3d, and (c) Co 2p XPS spectra of NF@NiMoCo after one-day HER and OER durability (CA) tests. The peaks of Ni^0 2p$_{3/2}$, Mo^0 3d$_{5/2}$, and Co^0 2p$_{3/2}$ retained well after HER, indicating the metallic state is dominated on the sample surface. The intensities of oxide/hydroxide peaks such as Ni^{2+}, Mo^{6+}, and Co^{2+} significantly increased after OER due to the oxidation process.

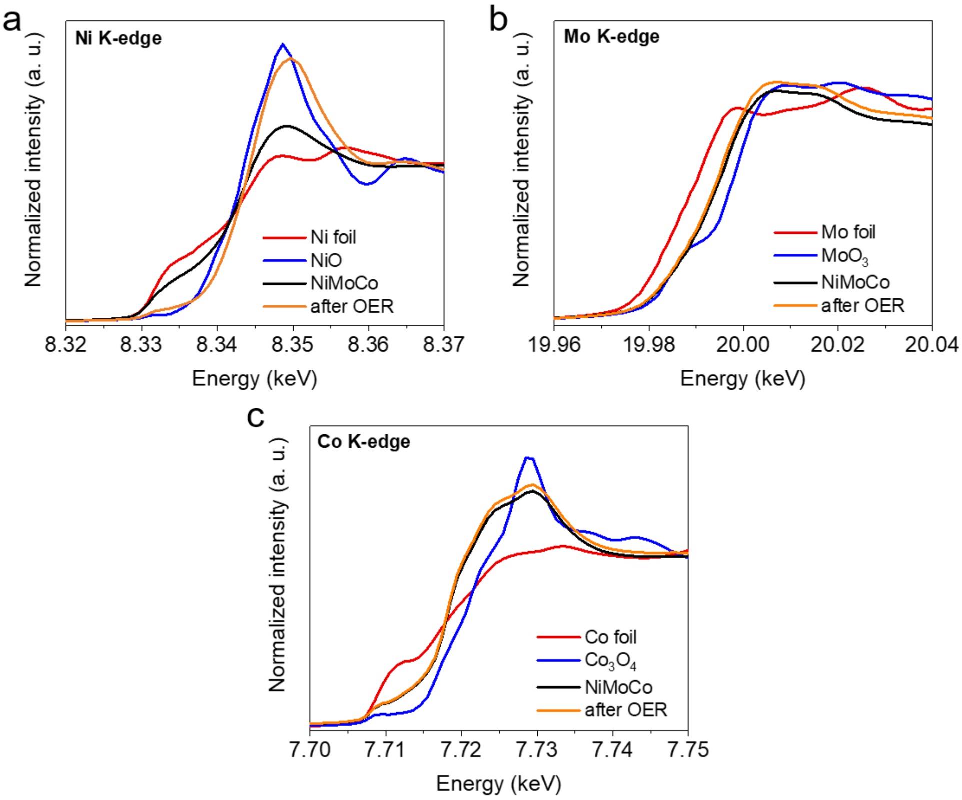

Figure S16. The XANES spectra of NiMoCo alloy nanowires and sample after OER test. The Ni showed an oxidation state after the OER test, while Mo and Co kept the similar chemical state with the initial sample, which is between the metal state (Mo, Co foil) and the highly oxided state (MoO_3, Co_3O_4).

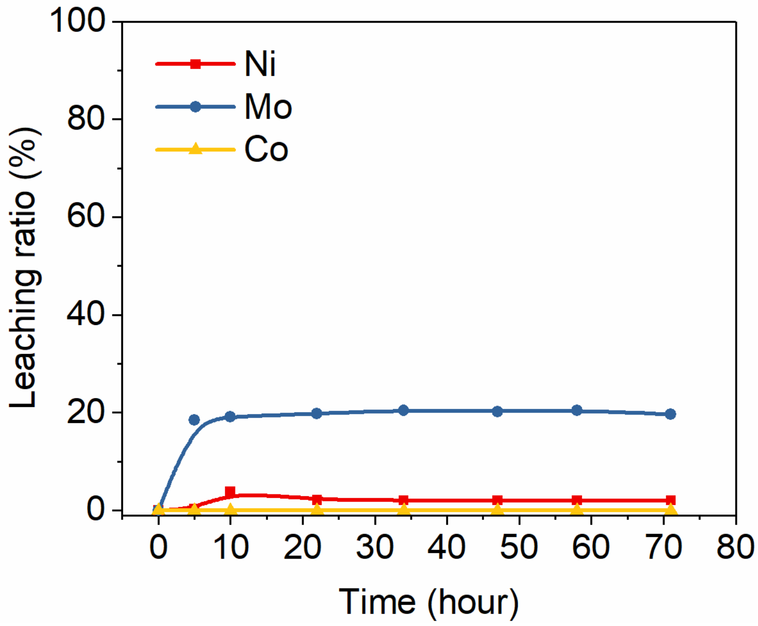

Figure S17. The Ni, Mo, and Co leaching ratios (wt.%) of NF@NiMoCo samples as both cathode and anode during overall water-splitting process.

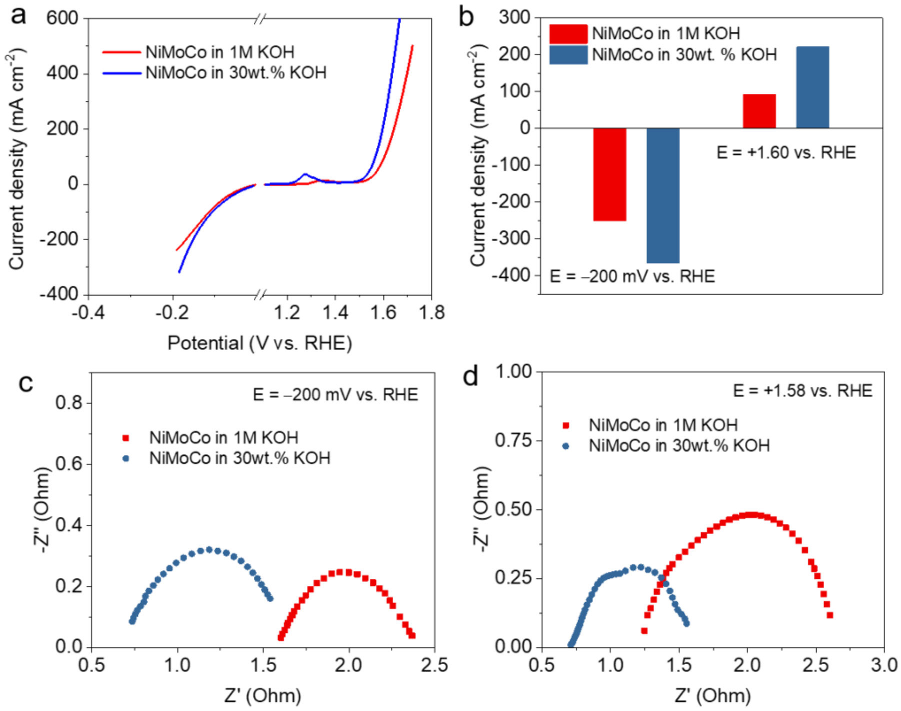

Figure S18. (a) HER/OER polarization curves, (b) performance summary and (c, d) Nyquist plots of NF@NiMoCo measured in 1.0 M KOH and 30 wt.% (7.64 M) KOH electrolytes.

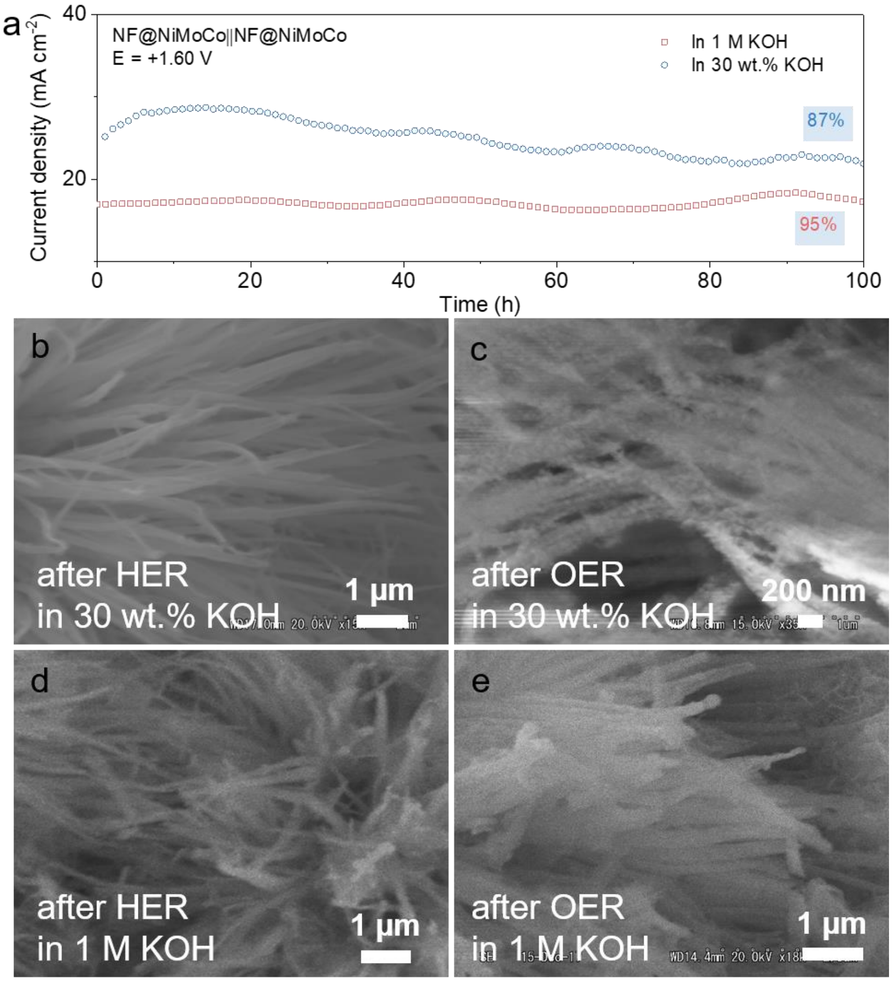

Figure S19. (a) The long-term water splitting test using a couple of NF@NiMoCo electrodes in 30 wt.% KOH and 1.0 M KOH electrolytes. SEM images of NF@NiMoCo after 24-hour CA test in (b, c) 30 wt.% KOH and (d, e) 1.0 M KOH electrolytes.

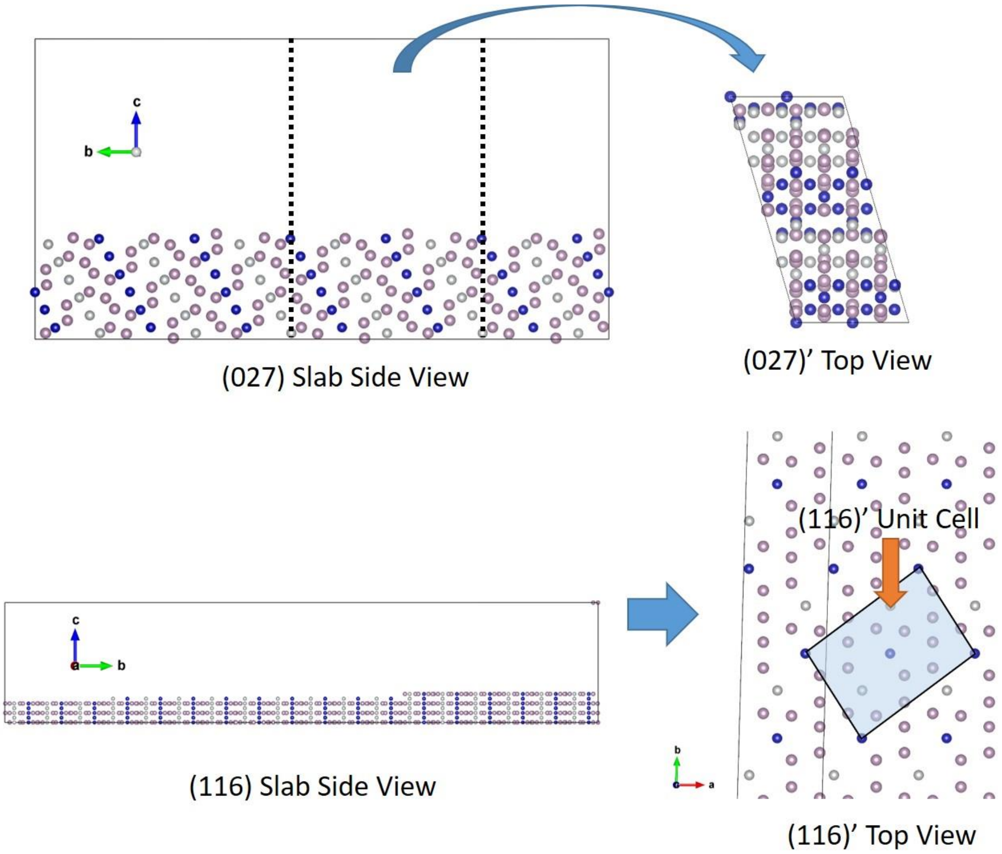

Figure S20. Side and top views of (027) and (116) surface slab models. Sliver, violet and blue balls represent Ni, Mo and Co atoms, respectively.

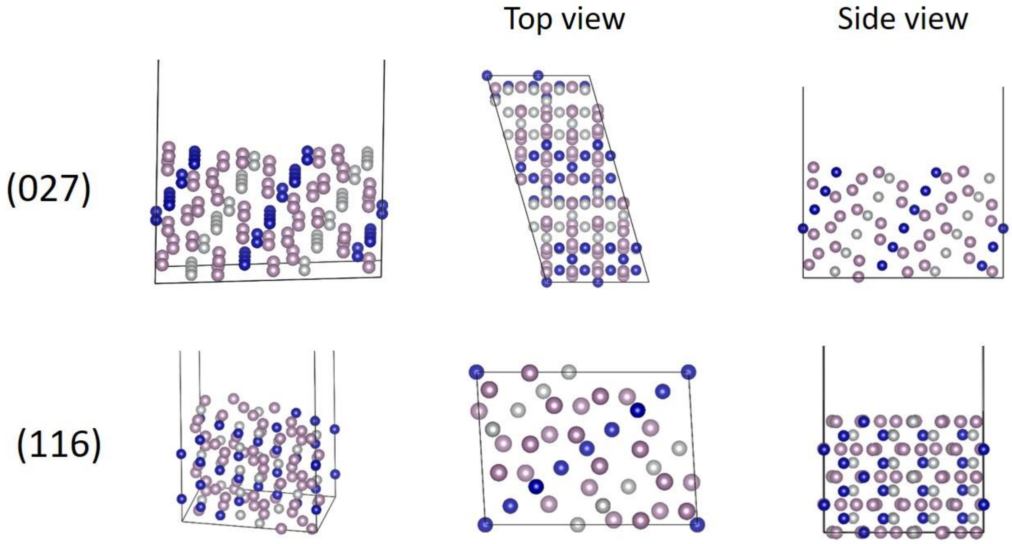

Figure S21. Side and top views of (027)' and (116)' surface slab models. Sliver, violet and blue balls represent Ni, Mo and Co atoms, respectively.

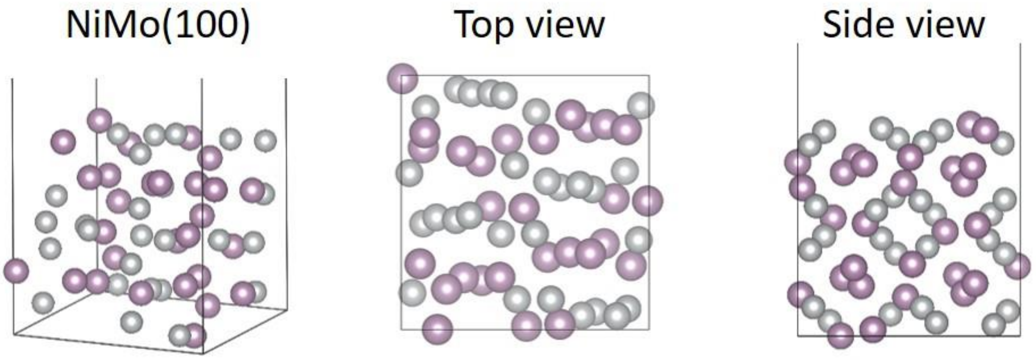

Figure S22. Side and top views of the NiMo(100) model. Sliver and violet balls represent Ni and Mo atoms.

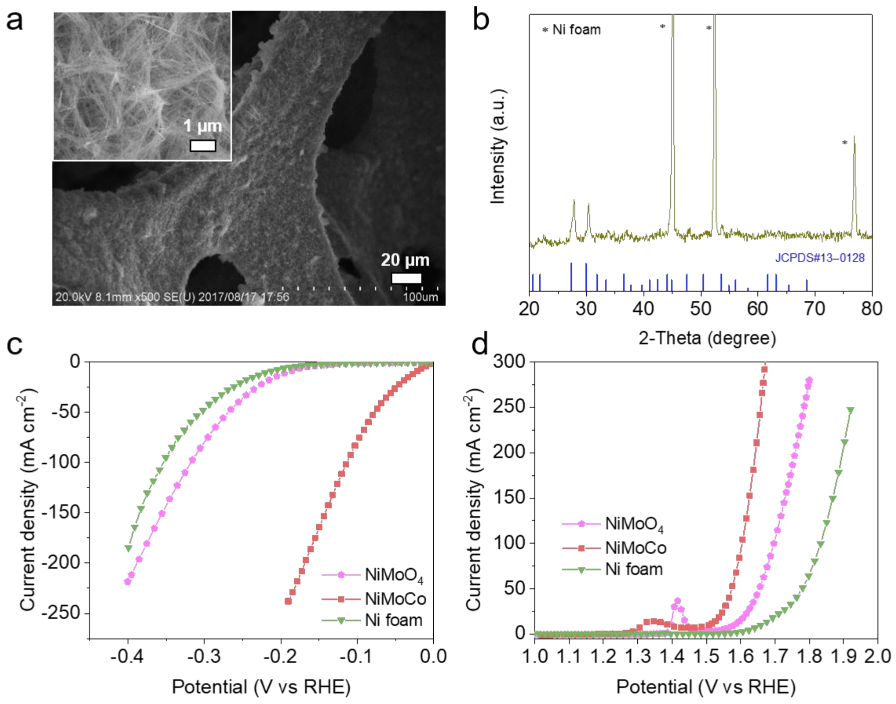

Figure S23. HER/OER activity of $NiMoO_4 \cdot xH_2O$ coated Ni foam (NF@$NiMoO_4$). (a) SEM images and (b) XRD pattern of NF@$NiMoO_4$. (c) HER and (d) OER polarization curves of NF@$NiMoO_4$.

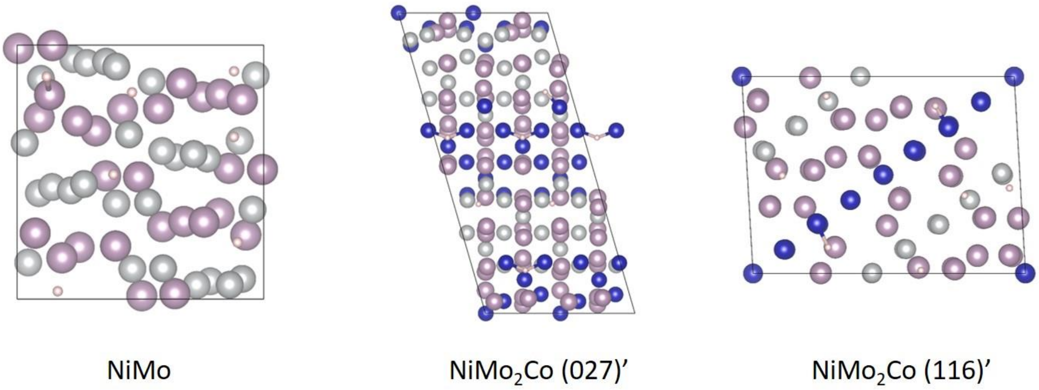

NiMo

$NiMo_2Co$ (027)’

$NiMo_2Co$ (116)’

Figure S24. Adsorption configurations of 6-7 hydrogen atoms on NiMo and $NiMo_2Co$ surfaces. The silver, violet, blue and small pink balls represent Ni, Mo, Co and H atoms, respectively.

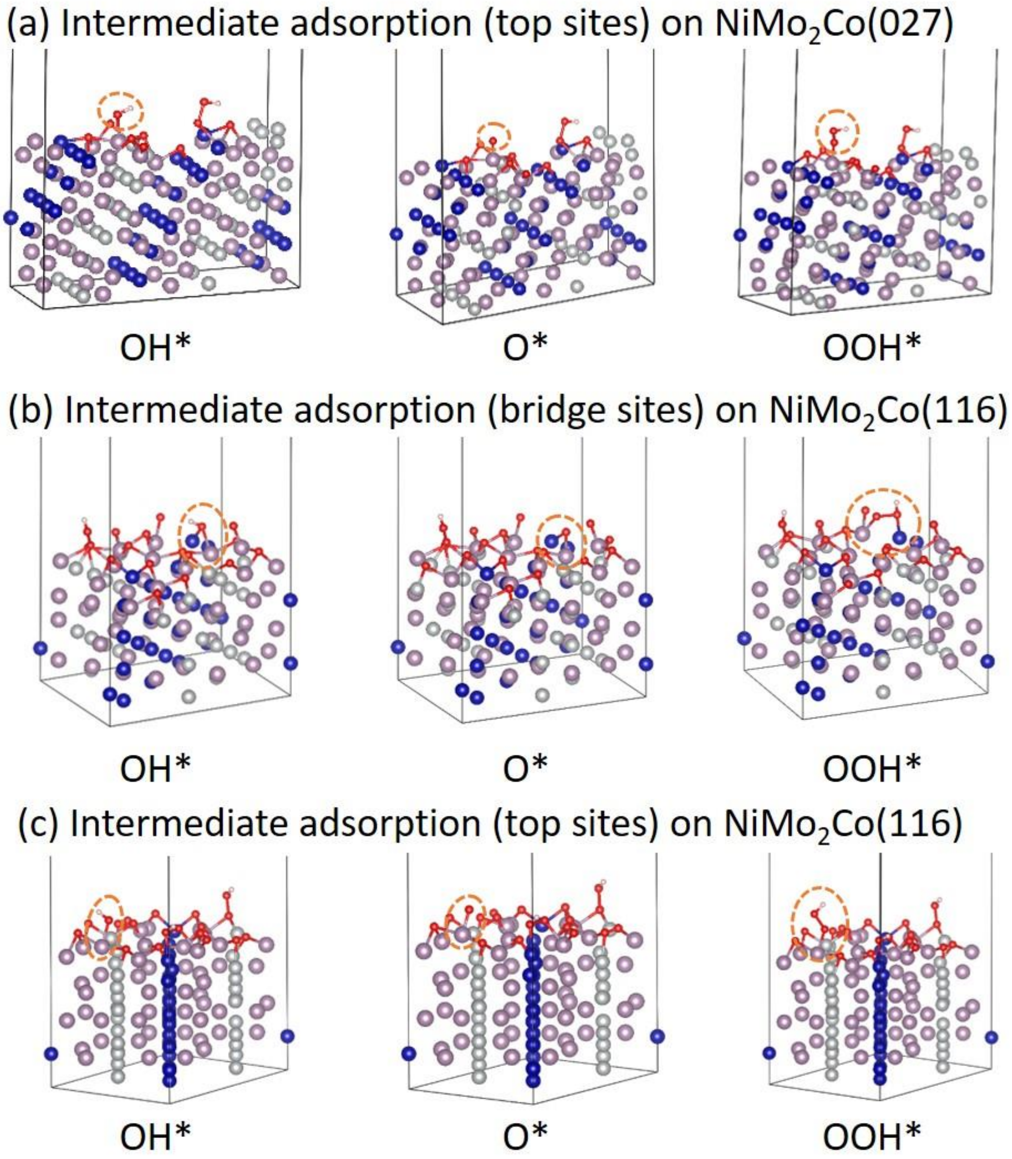

Figure S25. Adsorption configurations involved in the OER process on (a) the $NiMo_2Co$ (027) surface as top sites, on (b) the (116) surface as bridge sites and on (c) the (116) surface as top sites. The silver, violet, blue, red and small pink balls represent Ni, Mo, Co, O and H atoms, respectively. Orange circles show adsorption sites of each intermediate. Red balls without orange circles represent the oxygen atoms of self-generated oxides/hydroxides on the catalyst surface during OER process.

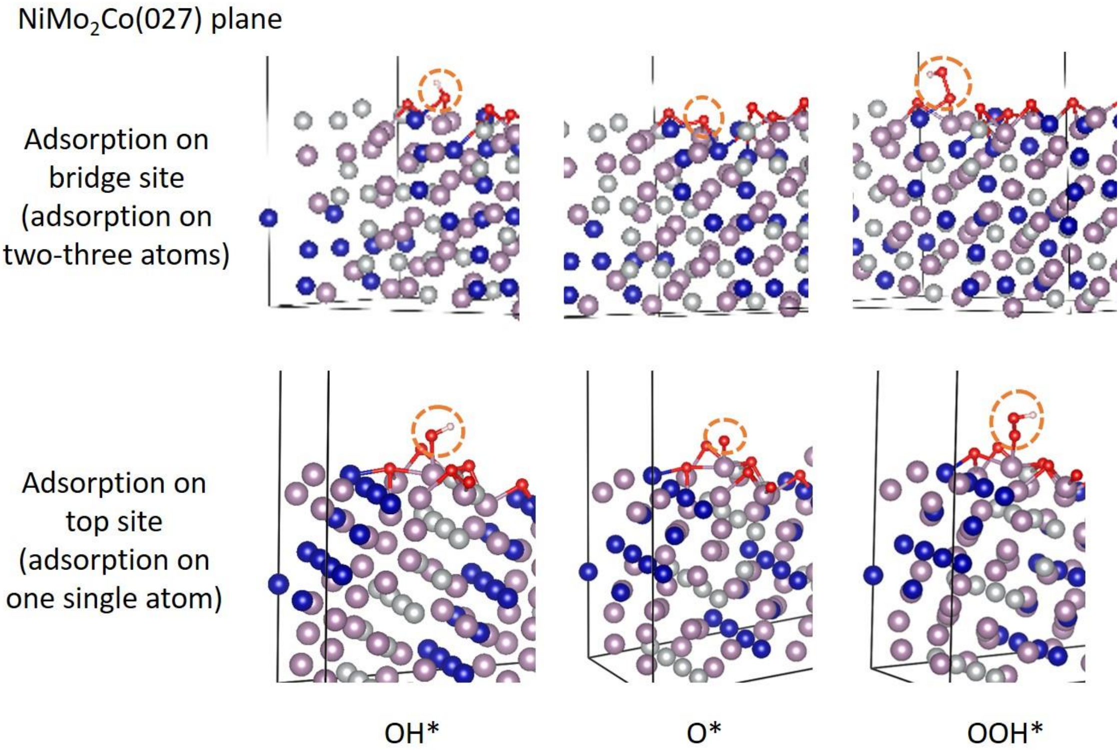

Figure S26. Two different intermediate adsorption types on the $NiMo_2Co(027)$ surface. Red balls without orange circles represent the oxygen atoms of self-generated oxides/hydroxides on the catalyst surface during OER process.

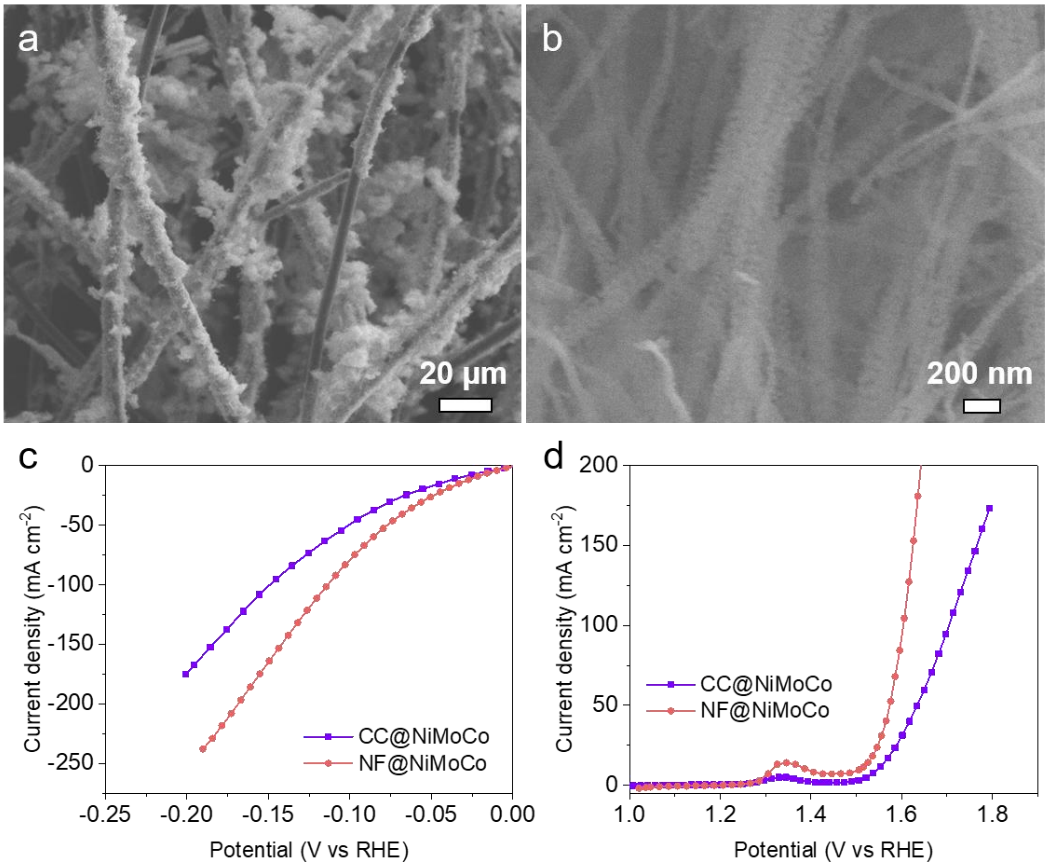

Figure S27. (a) Overview and (b) enlarged SEM images of NiMoCo alloy nanowire array coated on carbon cloth (CC@NiMoCo). (c) HER and (d) OER polarization curves of CC@NiMoCo and NF@NiMoCo.

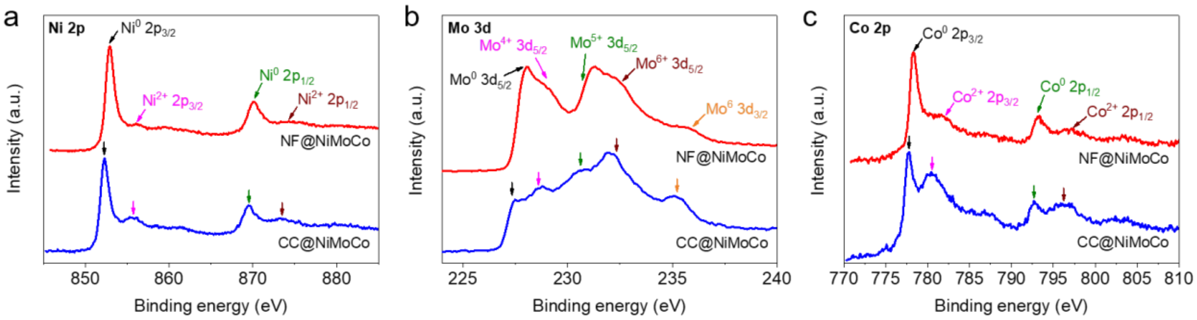

Figure S28. The high-resolution (a) Ni 2p, (b) Mo 3d, and (c) Co 2p XPS spectra of NiMoCo alloy nanowires coated on NF and CC substrates.

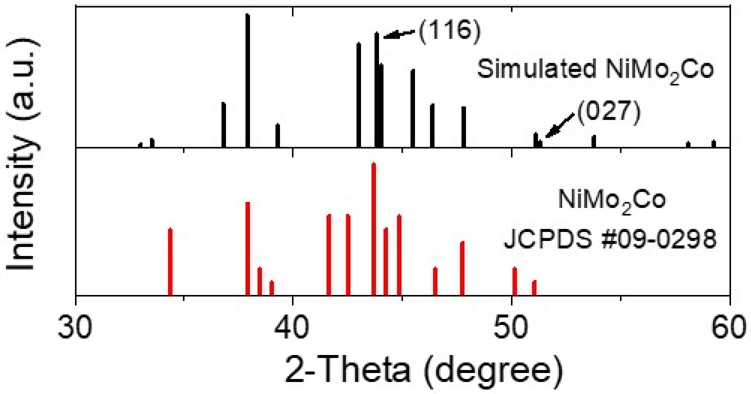

Figure S29. The simulated XPD pattern of $NiMo_2Co$ species for DFT calculations.

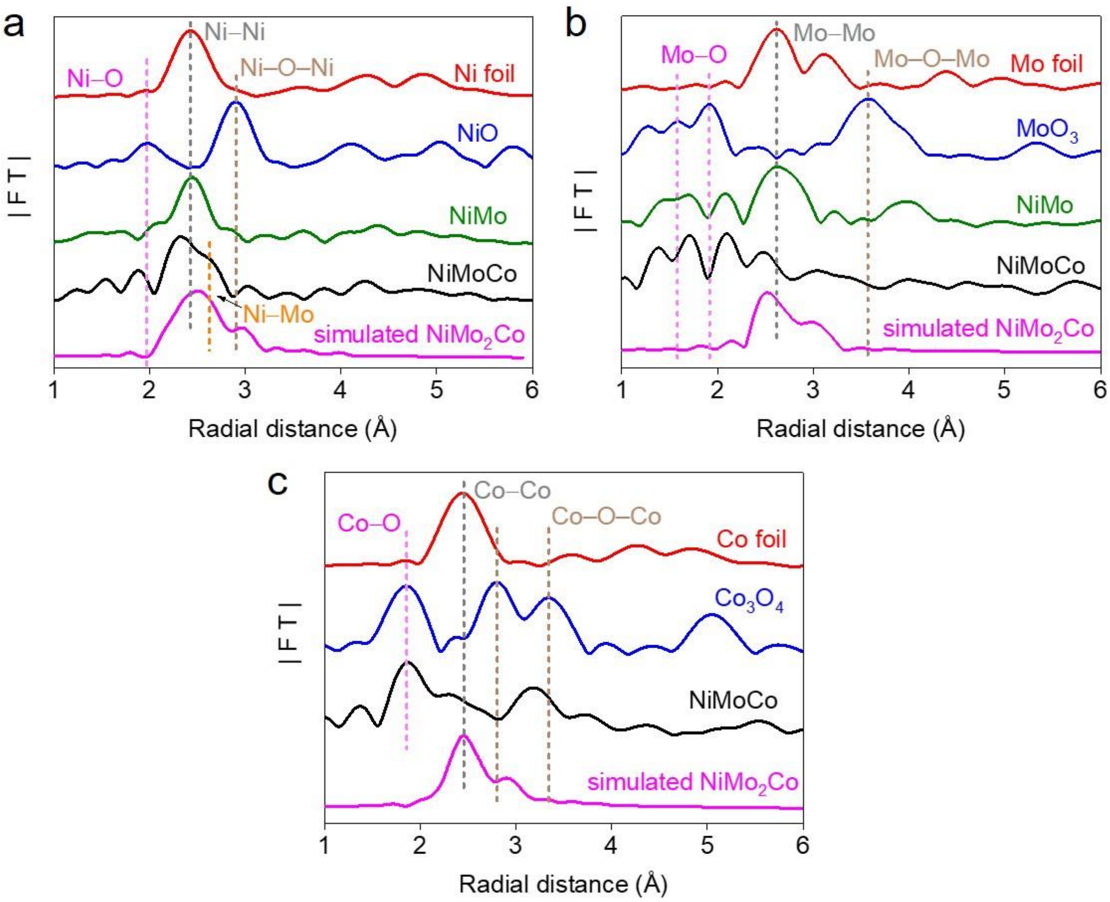

Figure S30. The simulated Fourier transformed magnitudes of the EXAFS data of $NiMo_2Co$ species for DFT calculations. FT curves of (a) Ni K-edge, (b) Mo K-edge, and (c) Co K-edge EXAFS.

Table S1. Comparison of HER performances for recently reported bifunctional catalysts.

Catalyst	$\eta_{10-\mathrm{HER}}$ (mV)	Tafel slope (mV dec^{-1})	Electrolyte	Reference
NF@NiMoCo	23	34	1.0 M KOH	This work
CC@NiMoCo	23	56	1.0 M KOH	This work
NF@NiMo	39	50	1.0 M KOH	This work
NF@MoCo	130	106	1.0 M KOH	This work
NF@NiCo	177	123	1.0 M KOH	This work
NiSe/NF	96	120	1.0 M KOH	Angew. Chem. Int. Ed., 2015, 54, 9351-9355
NF@CoFePO	87	38	1.0 M KOH	ACS Nano 2016, 10, 8738-8745
CC@NiCoFe LTHs	200	70	1.0 M KOH	ACS Energy Lett. 2016, 1, 445-453
NiFeMo	45	–	1.0 M KOH	ACS Energy Lett. 2018, 3, 546-554
NF@Ni/NiP	130	37.8	1.0 M KOH	Adv. Funct. Mater. 2016, 26, 3314-3323
$NiCo_2O_4$	110	49.7	1.0 M NaOH	Angew. Chem. Int. Ed. 2016, 55, 6290-6294
CoFeP	79	40	1.0 M KOH	Energy Environ. Sci., 2016,9, 2257-2261
Ni_3S_2/NF	223	–	1.0 M KOH	J. Am. Chem. Soc., 2015, 137, 14023-14026.
Cu@NiFe LDH	116	58.9	1.0 M KOH	Energy Environ. Sci., 2017, 10, 1820-1827
ceria/Ni-TMO/CC	93	69	1.0 M KOH	ACS Energy Lett. 2018, 3, 290-296
$Co_{0.9}S_{0.58}P_{0.42}$	139	72	1.0 M KOH	ACS Nano 2017, 11, 11031-11040

Table S2. Comparison of OER performances for recently reported bifunctional catalysts.

Catalyst	$\eta_{10\text{−OER}}$ (mV)	Tafel slope (mV dec^{-1})	Electrolyte	Reference
NF@NiMoCo	277	87	1.0 M KOH	This work
CC@NiMoCo	318	98	1.0 M KOH	This work
NF@NiMo	308	91	1.0 M KOH	This work
NF@MoCo	323	93	1.0 M KOH	This work
NF@NiCo	393	125	1.0 M KOH	This work
NiSe/NF	260	64	1.0 M KOH	Angew. Chem. Int. Ed., 2015, 54, 9351-9355
NF@CoFePO	274	52	1.0 M KOH	ACS Nano 2016, 10, 8738-8745
CC@NiCoFe LTHs	239	32	1.0 M KOH	ACS Energy Lett. 2016, 1, 445-453
NiFeMo	238	35	1.0 M KOH	ACS Energy Lett. 2018, 3, 546-554
NF@Ni/NiP	340	73.2	1.0 M KOH	Adv. Funct. Mater. 2016, 26, 3314-3323
$NiCo_2O_4$	290	53	1.0 M NaOH	Angew. Chem. Int. Ed. 2016, 55, 6290-6294
CoFeP	270	30	1.0 M KOH	Energy Environ. Sci., 2016,9, 2257-2261
Ni_3S_2/NF	260	–	1.0 M KOH	J. Am. Chem. Soc., 2015, 137, 14023-14026.
Cu@NiFe LDH	199	27.8	1.0 M KOH	Energy Environ. Sci., 2017, 10, 1820-1827
ceria/Ni-TMO/CC	210	38	1.0 M KOH	ACS Energy Lett. 2018, 3, 290-296
$Co_{0.9}S_{0.58}P_{0.42}$	266	69	1.0 M KOH	ACS Nano 2017, 11, 11031-11040

Table S3. Summary of ΔG values at the electrode potential of 0.0 V (vs. RHE).

	G(OH*), eV	G(O*), eV	G(OOH*), eV
NiMoCo027 (top site)	0.190	0.349	3.003
NiMoCo027 (bridge site)	0.798	1.000	3.899
NiMoCo116 (top site)	-0.297	0.376	2.966
NiMoCo116 (bridge site)	0.216	-0.063	4.284
NiMo100	0.417	0.643	3.568

Table S4. Comparison of overall water-splitting performances for recently reported bifunctional catalysts.

Catalyst	$E_{10-\text{water-splitting}}$ (cell voltage, V)	$E_{20-\text{water-splitting}}$ (cell voltage, V)	Electrolyte	Reference
NF@NiMoCo	1.56	1.60	1.0 M KOH	This work
NF@NiMo	1.62	1.67	1.0 M KOH	This work
NF@MoCo	1.69	1.75	1.0 M KOH	This work
NF@NiCo	1.78	1.84	1.0 M KOH	This work
NiSe/NF	1.63	1.74	1.0 M KOH	Angew. Chem. Int. Ed., 2015, 54, 9351-9355
NF@CoFePO	1.56	~1.64	1.0 M KOH	ACS Nano 2016, 10, 8738-8745
CC@NiCoFe LTHs	1.55	1.63	1.0 M KOH	ACS Energy Lett. 2016, 1, 445-453
NiFeMo	1.45	~1.58	1.0 M KOH	ACS Energy Lett. 2018, 3, 546-554
NF@Ni/NiP	1.61	~1.68	1.0 M KOH	Adv. Funct. Mater. 2016, 26, 3314-3323
$NiCo_2O_4$	1.65	1.74	1.0 M NaOH	Angew. Chem. Int. Ed. 2016, 55, 6290-6294
CoFeP	1.53	~1.59	1.0 M KOH	Energy Environ. Sci., 2016,9, 2257-2261
Ni_3S_2/NF	1.75	–	1.0 M KOH	J. Am. Chem. Soc., 2015, 137, 14023-14026.
Cu@NiFe LDH	1.54	~1.58	1.0 M KOH	Energy Environ. Sci., 2017, 10, 1820-1827
ceria/Ni-TMO/CC	1.58	~1.59	1.0 M KOH	ACS Energy Lett. 2018, 3, 290-296
$Co_{0.9}S_{0.58}P_{0.42}$	1.59	~1.62	1.0 M KOH	ACS Nano 2017, 11, 11031-11040

Table S5. The scattering path for Ni K-edge FT-EXAFS.

Samples	Shell	r/Å [a]	CN [b]
$NiMo_2Co$	Ni−Ni	2.37	4.0
	Ni−Mo	2.58	1.0
	Ni−Mo	2.63	3.0
	Ni−Mo	2.79	2.0
	Ni−Mo	2.82	1.0
Ni metal (foil)	Ni−Ni	2.49	12.0
NiO	Ni−O	2.08	6.0
	Ni−O−Ni	3.00	12.0

Interval of *k*-space to *r*-space of FT is 3.0−15.0 $Å^{-1}$.

[a] Atomic distance.

[b] Coordination number.

Reference

[1] F. Song and X. L. Hu, *Nat. Commun.*, 2014, 5, 4477.

[2] G.-F. Chen, T. Y. Ma, Z.-Q. Liu, N. Li, Y.-Z. Su, K. Davey and S. Z. Qiao, *Adv. Func. Mater.*, 2016, 26, 3314−3323.

[3] J. Wang, F. Xu, H. Y. Jin, Y. Q. Chen and Y. Wang, *Adv. Mater.*, 2017, 29, 1605838.

[4] C. Tang, N. Y. Cheng, Z. H. Pu, W. Xing and X. P. Sun, *Angew. Chem. Int. Ed.*, 2015, 127, 9483−9487.

[5] G. Kresse and J. Hafner, *J. Phys.: Condens. Matter*, 1994, 6, 8245.

[6] P. E. Blöchl, *Phys. Rev. B*, 1994, 50, 17953-17979.

[7] J. P. Perdew, K. Burke and M. Ernzerhof, *Phys. Rev. Lett.*, 1996, 77, 3865-3868.

[8] S. Grimme, J. Antony, S. Ehrlich and H. Krieg, *J. Chem. Phys.*, 2010, 132, 154104.

[9] S. Grimme, S. Ehrlich and L. Goerigk, *J. Comput. Chem.*, 2011, 32, 1456-1465.

[10] Y. Ito, T. Ohto, D. Hojo, M. Wakisaka, Y. Nagata, L. H. Chen, K. L. Hu, M. Izumi, J.-i. Fujita and T. Adschiri, *ACS Catalysis*, 2018, 8, 3579-3586.

[11] C. B. Shoemaker and D. P. Shoemaker, *Acta Crystallographica*, 1963, 16, 997-1009.

[12] Y. Wang, C. Woodward, S. H. Zhou, Z. K. Liu and L. Q. Chen, *Scripta Materialia*, 2005, 52, 17-20.

[13] T. Ishchenko and L. Meshkov, *Vestn. Mosk. Univ., Khim.*, 1983, 24, 567.

[14] Y. Wang, P. Gao, X. Wang, J. Huo, L. Li, Y. Zhang, A. A. Volinsky, P. Qian and Y. Su, *Physical Chemistry Chemical Physics*, 2018, 20, 14545-14556.

[15] L. C. Seitz, C. F. Dickens, K. Nishio, Y. Hikita, J. Montoya, A. Doyle, C. Kirk, A. Vojvodic, H. Y. Hwang, J. K. Norskov and T. F. Jaramillo, *Science*, 2016, 353, 1011-1014.

[16] J. H. Wang, W. Cui, Q. Liu, Z. C. Xing, A. M. Asiri and X. P. Sun, *Adv. Mater.* 2016, 28, 215−230.

[17] S. Anantharaj, S. R. Ede, K. Sakthikumar, K. Karthick, S. Mishra and S. Kundu, *ACS Catal.* 2016, 6, 8069−8097.

[18] N.-T. Suen, S.-F. Hung, Q. Quan, N. Zhang, Y.-J. Xu and H. M. Chen, *Chem. Soc. Rev.* 2017, 46, 337−365.

[19] L. Yu, H. Q. Zhou, J. Y. Sun, F. Qin, F. Yu, J. M. Bao, Y. Yu, S. Chen and Z. F. Ren, *Energy Environ. Sci.*, 2017, 10, 1820−1827.

[20] C. Tang, N. Y. Cheng, Z. H. Pu, W. Xing and X. P. Sun, *Angew. Chem. Int. Ed.*, 2015, 127, 9483−9487.

[21] Y.-Y. Chen, Y. Zhang, X. Zhang, T. Tang, H. Luo, S. Niu, Z.-H. Dai, L.-J. Wan and J.-S. Hu, *Adv. Mater.*, 2017, 29, 1703311.

[22] J. J. Duan, S. Chen, A. Vasileff and S. Z. Qiao, *ACS Nano*, 2016, 10, 8738−8745.

[23] X. H. Gao, H. X. Zhang, Q. G. Li, X. G. Yu, Z. L. Hong, X. W. Zhang, C. D. Liang and Z. Lin, *Angew. Chem. Int. Ed.*, 2016, 55, 6290−6294.

[24] Y. W. Tan, H. Wang, P. Liu, Y. H. Shen, C. Cheng, A. Hirata, T. Fujita, Z. Tang and M. W. Chen, *Energy Environ. Sci.*, 2016, 9, 2257−2261.

[25] X. Long, H. Lin, D. Zhou, Y. M. An and S. H. Yang, *ACS Energy Lett.*, 2018, 3, 290−296.

[26] Z. F. Dai, H. B. Geng, J. Wang, Y. B. Luo, B. Li, Y. Zong, J. Yang, Y. Y. Guo, Y. Zheng, X. Wang and Q. Y. Yan, *ACS Nano*, 2017, 11, 11031−11040.